Model for (a)synchronous/spontaneous release, applied to CCK-positive Interneuron synapses

Serafim Rodrigues,[1*†] Mathieu Desroches,[2*], Martin Krupa[2*], Jesus M Cortes[3,4] and Afia B Ali[5*]

[1]School of Computing and Mathematics, Centre for Robotics and Neural Systems, Plymouth University, UK,

[2]SISYPHE Project-Team, INRIA Paris-Rocquencourt Research Centre, France,

[3]Ikerbasque, the Basque Foundation for Science, Bilbao, Spain

[4]Biocruces Health Research Institute, Hospital Universitario de Cruces, Barakaldo, Spain

[5]UCL School of Pharmacy, Department of Pharmacology, University College London, UK.

[*] These authors have contributed equally.

[†] To whom correspondence should be addressed: serafim.rodrigues@plymouth.ac.uk

One Sentence Summary: A novel multi-timescale model offers a unified framework to explain short-term synaptic plasticity as well as asynchronous, synchronous and spontaneous neurotransmitter release as observed at synapses involving cholecystokinin-positive neurons.

Asynchronous and spontaneous neurotransmitter release remain elusive and constitute topics of considerable research both from the experimental and modeling perspective. This study proposes a parsimonious model that accounts for all modes of vesicle exocytosis and Short-Term Synap-

tic Plasticity (STSP). The modeling novelty is based on principles of slow-fast dynamical systems theory. The model's validity is shown by its good agreement with experimental data obtained from in vitro electrophysiological dual whole-cell recordings between local cholecystokinin (CKK)-positive, Schaffer collateral associated (SCA) interneurons in the CA1 region of rat hippocampus (*1, 2*). These unitary synapses display asynchronous release, governed by the retrograde release of endocannabinoid in response to post-synaptic membrane depolarisation. This work will advance our understanding of the physiology underlying differential exocytosis, and facilitate large-scale neuronal simulations.

Introduction. Increasingly, molecular and electrophysiological data point to differences between the regulation of pre-synaptic exocytotic machinery for elicited (synchronous or asynchronous) and spontaneous neurotransmitter release. Synchronous release initiates within a millisecond after an action potential, induces calcium influx and, subsequently, calcium-mediated membrane fusion (synaptotagmin, SNARE proteins, SM-protein and complexin) (*3*). Asynchronous release, which manifests itself only under certain conditions, sets in with a longer delay after an incoming action potential (*3,4*). Finally, spontaneous "mini" release occurs in the absence of an action potential (*4*). In particular, asynchronous and spontaneous modes remain poorly understood and consequently have inspired, in the recent years, many important molecular and computational studies (*4–9*). These studies propose two distinct mechanisms to explain the various modes of exocytosis. The more parsimonious view, supported by some experimental evidence (*10, 11*), is that asynchronous and spontaneous release share in part the same exocytosis machinery that regulates synchronous release. The competing and more recent view, which is supported by new lines of experimental evidence, suggests distinct signalling pathways and

possibly independent vesicle pools. As a case in point, Ca^{2+}-sensor Doc2, which binds Ca^{2+} with slower kinetics, has been identified for excitatory neurons (*5*), while for inhibitory neurons Ca^{2+}-sensor VAMP4, phosphoprotein isoforms Synapsin (Syn I and Syn II) and endocannabinoids seem to regulate asynchronous release (*2, 6, 12*). These views are still being debated due to fragmentary and conflicting data. For example, a recent work challenges the legitimacy of Doc2 as a calcium sensor for asynchronous release (*13, 14*).

Model assembly. As a first step towards resolving some of the divergent views, the present study proposes a mathematical model that reproduces all three modes of neurotransmitter release as observed at unitary synapses. The model formulation differs from previous modelling attempts that employ stochastic terms to account for asynchronous release (*7–9*). It also refrains from hardwiring a delay into the model, but rather uses a dynamic mechanism that is suggestive of a biological process. Specifically, a novel approach based on slow-fast dynamical systems theory (*15*) is used, which allows to express features of slow, evoked irregular and spontaneous activation. This yields a two-dimensional nonlinear deterministic differential equation (Markovian); see Fig. 1 (B). The model variables (p_1, p_2), which can be activated by a pre-synaptic stimulus $V_{in}(t)$, may be thought of as representing (at a mesoscopic scale) a cascade of protein-protein interactions that mediate the functions associated with the exocytosis-endocytosis signalling pathway, including the activation of a vesicle pool. To facilitate the description, the model will be henceforth denoted the Vesicle Activation (VA) model. In the model, p_1 is a slow acting protein complex, while p_2 is a fast complex. The three release modes are mediated by key control parameters that regulate not only the interaction strength between p_1 and p_2, but also the conformational changes of the individual protein complexes. In particular, the interaction between p_1 and p_2 generate special configuration points, namely S (*stable equilibrium*), U (*unstable equilibrium of saddle type*), SN (*saddle-node* point) and TC (*transcritical* point) (see

Fig. 2 (A) and subsequent sections for details), which generate all the functions associated with each stage of the exocytosis-endocytosis cycle. Crucially, the VA-model is sensitive to initial conditions without featuring chaos. This sensitivity constitutes the core mechanism that governs the irregular activation. Moreover, due to the timescale separation between p_1 and p_2, the delayed release results from the binding (attraction towards the TC point) and subsequent unbinding that occurs with inertia, which is precisely what quantifies the delay. Technically, this delay process is the so-called *dynamic transcritical bifurcation* and the associated trajectories are an example of *canard orbits* (*16*) (see Supporting Online Material - SOM). Interestingly, the VA-model has a mechanistic interpretation since it can be related to processes associated with exocytosis-endocytosis signalling pathways, which include intracellular calcium dynamics. Moreover, the delayed irregular activation may be related to the action of VAMP4, Syn I (II), the presence of endocannabinoid, or even Doc2 in the case of excitatory neurons. As shown in Fig. 1, the output of the VA-model feeds into the Markram-Tsodyks (MT) model (*17*). Briefly, the MT equations phenomenologically model the time-evolution of available resources (vesicles) and how efficiently neurotransmitters are released. This is represented by two quantities, namely, the amount of vesicles, d, and the release probability, f, which are updated for every pre-synaptic spike occurring at time instant t_s. This in-turn quantifies the amount of neurotransmitter released, $T(t_s) = d(t_s)f(t_s)$, which in reality is released with a small time delay. The MT-model successfully accounts for the highly heterogeneous STSP dynamics across different brain areas in the context of synchronous release (see Table S1 in (*18*)). Consequently, the proposed model extends the MT-model by incorporating the other modes of release. However, to complete the model framework and to enable testing against paired-recording data obtained from unitary synapses, an observational variable representing post-synaptic potentials is required. This is modelled with the standard conductance-based (sub-threshold) equation, where the GABA_A-receptor conductance g_{gaba} follows a first-order kinetic equation (see Fig. 1

(B)). Thus the modulation of p_2 onto neurotransmitters (T) enables receptor activation. The receptor deactivation is followed by the unbinding of neurotransmitters from the receptor, which occurs with a finite decay-time. More detailed approaches for modelling receptor dynamics (e.g. detailed kinetics (*19*) or using M-Cell simulator (*20*)) will be a matter of future considerations. Henceforth, to facilitate description, the proposed complete set of equations will be denoted the VAMT-g model.

VA-model dynamics. The VA-model's signalling mechanism and its three operating modes are subsequently discussed. Fig. 2 (A) shows a pre-synaptic neuron, which encapsulates the VA-model's signalling mechanism. The black arrows labeled p_1 and p_2 display the two-dimensional space within which the protein complexes interact. This is not a physical space, but rather a space where protein functions take place (technically, *phase-space*). The horizontal half-line and the half-parabola (black) indicate the regions in which the functions of the protein complexes are stationary and stable (technically, *fast nullclines*); see Fig. S1. However, these can become unstable at the transitions marked by points SN and TC, and subsequent switches to dashed lines. For convenience, the *slow nullclines* are not displayed; see SOM for details. To understand the VA-model's evolution, the case when p_1 is kept constant (fixed configuration) is first considered. When this occurs, p_2 evolves alone towards a special state, which is attracting for fixed configuration of p_1 up to the transitional configuration TC, and repelling past this transition. In normal operating conditions, when p_1 evolves slowly, the VA-model possesses two true stationary states, marked S and U (intersections of the slow and fast nullclines, see Fig. 2 and SOM). An exocytosis signal (red trajectory) is evoked via one (or several) pre-synaptic spike(s). Input stimuli excite the system away from the functionally-inactive state S and the TC configuration enables the appropriate exocytotic signalling mode to be activated. However, only sufficient energy (possibly related to calcium influx) allows the protein complexes to switch their functional

behaviour past the switching point (U). Fig. 2 illustrates the same information in the time domain: panel (B1) shows the pre-synaptic stimuli and panel (B2) the output signal. An analogy is made in panel (B3), which depicts a particle that is initially at a rest point (S); sufficient forcing (blue arrows) then drives the particle away from the basin of attraction of S enabling it to jump the energy barrier (U). This scenario, in which a particular amplitude and timing of a perturbation drives the system away from an equilibrium and induces it to make a transient large-amplitude excursion before it settles again to its inactive state, is called *excitable* (*15*).

Past the switching point (U), the protein complexes p_1 and p_2 begin to strongly interact, which can be related to the activation of protein functions associated to vesicle docking, with unassembled SNARE complexes (compare to Fig. 3 in (*3*)). The passage through the TC point initiates the priming stage (P) and it can be linked to functions associated to SNARE-complex assembly (see Fig. 3 in (*3*)). Priming can be a fast process (synchronous mode) or a slow process (asynchronous mode), depending on the modulation of the parameter ε. More precisely, from the mathematical viewpoint, a precise quantitative control of the delay is achieved by the so-called *way-in-way-out function* (see SOM). The parameter ε controls the timescale separation between p_1 and p_2, modulating both the level of reciprocal interaction (binding) and subsequent unbinding that can occur with inertia, i.e., with a delay. Moreover, ε may encode the action of endocannabinoid, or associated (a)synchronous calcium sensors. The unbinding of p_1 and p_2 initiates the fusion stage (F), where neurotransmitters are immediately released. Following the exocytosis process, p_1 and p_2 begin a second phase of strong interaction that induces endocytosis (E) and subsequent vesicle refilling (R). The final stage is triggered by the SN (switch) state, which prompts p_1 and p_2 to alter their states and have a transition towards their inactive state S, where the vesicle pool is replenished.

The model's mechanisms for the differential modes of exocytosis are subsequently discussed; all parameters are given in Table S1 of the SOM. Fig. 3 exemplifies evoked (synchronous and asynchronous) output modes of the VA-model. For the synchronous mode, panel (A) shows that the VA-model's output, p_2, is activated almost instantaneously upon incoming stimulus, V_{in}. In this case, ε has a small value. In contrast, increasing ε induces a weaker binding/unbinding. This effectively introduces variability (irregular activation via sensitivity to initial conditions) and a strong inertia in the unbinding process, which causes the delay. Panel (B) exemplifies the asynchronous mode, where the onset of p_2 is delayed with respect to the stimulus. Note that the output time profile changes shape and amplitude, and has a slower response. These are crucial features that lead to gradual activation of vesicle pools as well as post-synaptic receptors, which is consistent with the gradual post-synaptic potential response observed in experiments for asynchronous release (*3*). Panel (C) shows three different delayed responses under the same two-spike stimulus, which demonstrates the model's sensitivity to initial conditions that underlies irregular activation. Moreover, a burst of spikes may be required before the vesicle pool is activated, which is also a feature widely reported in experiments (*3*). This feature is controlled by increasing the distance between the two configuration states S and U, which has the effect of increasing the energy barrier (see Fig. 2 (B3)). The further they are apart, the stronger the stimulus (multiple spikes) is needed to elicit vesicle priming (P). As an example, a delayed response to a stimulus of three spikes is shown in panel (D). Note that if the inter-spike interval between the input stimuli is smaller (larger frequency) when compared to a typical exocytotic-endocytotic cycle time, then the delay decreases proportionally to the input frequency increase. However, this delay does not decrease below a fixed value that corresponds to a synchronous release.

Finally, spontaneous release is now discussed. There are two different ways to generate spon-

taneous "mini" releases in the VA-model, illustrated in Fig. 3 panels (E) and (F), respectively. One way is to assume that Ca^{2+}-channels open stochastically, which changes the resting baseline of Ca^{2+}-concentrations (*4*). In this scenario, the model is tuned to narrow down the amplitude of the parabola (nullcline), which changes the fusion dynamics. This change can be related to experimental observations, for example, empirical data showing the existence of multiple-fusion processes, namely the *kiss-and-run*, *clatherin-dependent endocytosis* and *bulk endocytosis* (*21*). Relevant to spontaneous release is the *kiss-and-run* mechanism, where vesicles do not fuse entirely with the membrane and thus are rapidly retrieved from the active zone (release site). Moreover, the model is also tuned to be in a strongly excitable regime, which corresponds to placing the two configuration states S and U sufficiently close. As a consequence, small-noise perturbation is sufficient to perturb the model's dynamics away from its inactive state (S) and to have a complete "priming/fusion/*kiss-and-run* endocytosis" excursion in phase-space before it settles back to S; see Fig. 3 (E). An alternative mode of spontaneous release is to assume Ca^{2+}-sparks via Ca^{2+}-influx from internal Ca^{2+}-stores (*3, 4*). In this scenario, the model features a *limit cycle* (a self-sustained periodic signal), which can resemble internal calcium stores that allow for self-sustained oscillations; see Fig. 3 (F). This is achieved by moving both the S and U configuration points to the far left; as a consequence signals emanating from the SN point no longer fall into the basin of attraction of S, prompting another exocytotic-endocytotic cycle. The limit cycle can have an irregular period by random variation of its associated parameters (see SOM).

VAMT-g model predictions. The validity of the full model is subsequently demonstrated against experimental data. In particular, the data is sampled from paired whole-cell recordings obtained from unitary synapses between CCK-positive SCA interneurons in the CA1 region of P18-21 rat hippocampus (*1, 2*) (see Fig. 4 and experimental details in SOM). These cells pos-

sess a modulatory feedback mechanism that allows the post-synaptic cell to control the level of pre-synaptic $GABA_A$ release via the endocannabinoid (eCB) system, which is composed of cannabinoid receptors, ligands and the relevant enzymes (*1, 2*). Specifically, endocannabinoid, 2-arachidonoyglycerol (2-AG) or anandamide is synthesised and released on demand, involving depolarisation of the postsynaptic membrane via the activation of voltage-dependent L-type calcium channels (*22*). Once synthesised it diffuses across the synaptic cleft to modulate the activation of cannabinoid type 1 (CB1) receptors located in the pre-synaptic cell. Subsequently, CB1 receptors inactivate N-type (and possibly P/Q type) calcium channels (therefore reducing Ca^{2+} concentration) leading to a reduction of $GABA_A$ release (*1, 2, 23, 24*). Experimentally, the level of CB1 receptor activation and deactivation was controlled by bath application of endogenous agonist, anandamide and antagonist, AM-251. The endogenous agonist effects could be mimicked by depolarisation-induced suppression of inhibition (DSI) protocols, which involved depolarisation of the postsynaptic membrane (*1, 2*). These modulatory synaptic effects have a direct impact on the timing of synaptic inhibition, specifically, asynchronous release and STSP; see Fig. 4. To replicate these observations, experimental parameters along with parameters associated to $GABA_A$-induced currents were extracted from (*1, 25, 26*); the MT-model parameters were adopted from (*17,18*). The VA-model parameters were adjusted to generate the appropriate release mode (see Table S1 in SOM). The remaining parameters were tuned within a bounded region (see Table S2 in SOM). Fig. 5 demonstrates that the VAMT-g model successfully reproduces experimental data. The top two panels compare a delayed unitary inhibitory post-synaptic potential (uIPSP) (A1) with model's output (B1). The middle two panels compare a sequence of IPSPs possessing short-term synaptic depression and delayed responses (A2), which results from multiple pre-synaptic stimulation, with the model's output (B2). The bottom panels compare the data (A3), which display a sequence of IPSPs featuring short-term synaptic facilitation and delayed responses, with the model (B3). Consistently the model shows quantitive agreement for

the onset of the delays and a qualitative agreement with the time profile of IPSPs; this is also verified with other data sets (not shown). Specifically to delayed release, note that more care should be taken in the model fitting. Since the model is sensitive to initial conditions (for a given value of ε that induces a certain delay and variability) then a completion of an exocytotic-endocytotic cycle brings the system to a different configuration. This implies that parameters of the previous exocytotic-endocytotic cycle will give rise to different delayed response upon a new stimulus. This can be understood as representing the changes in the exocytotic-endocytotic signalling pathways that occur between the subsequent release cycles. Parameters associated to $GABA_A$-induced currents also undergo changes, albeit minor, since endocannabinoids increase the input resistance of the cell, docking time of neurotransmitters and affinity. Parameters of the MT-model also change reflecting the transition from one mode of release to another. Consequently, effective model fitting must be carried out by fitting epochs of data for incoming stimuli associated to different modes of release and ensuring that continuity conditions are satisfied. These conditions occur between the epochs marked by the shaded magenta rectangle and the shaded cyan rectangle; see Fig. 5 (A2,B2,A3,B3). Future developments will include the conditions ensured by the *way-in-way-out* function for an automatic parameter fitting. However, in the limit of complete depletion of neurotransmitters, fitting any continuous macroscopic model to electrophysiological data becomes increasingly difficult, because noise dominates and expressing microscopic dynamics becomes fundamental. In this limit, other theoretical studies reveal that discrete, stochastic or agent-based models best describe microscopic activity (*27*).

Discussion. We introduce a multiple-timescale model of the exocytosis-endocytosis cycle activation extending the MT framework; it incorporates all three forms of exocytosis while keeping the same level of description. Its phenomenological nature implies that details of the biochemical pathways involved in exocytosis are not explicitly expressed. Instead, a mesoscopic view is

adopted, yet the model can be mapped to exocytotic-endocytotic physiology and its dynamics, to exocytotic-endocytotic functions. Therefore, it can be used to formulate new computational and experimental hypotheses, and its use may suggest novel experiments. Its minimal structure is a starting point for further developments. For instance, in every exocytosis-endocytosis cycle, the release mode may switch due to yet unknown slowly-varying quantities; these aspects are not modelled and are considered as model parameters. The mesoscopic model's description predicts that distinct forms of release may share in part the same exocytosis machinery, where specific parameters dictate the desired exocytosis mode. However, it is important to be cautious since parameters may encode different pathways.

Our results are consistent with recent studies showing that Syn I(II), known to coat synaptic vesicles and to have some post-docking role, cooperate to regulate (a)synchronous release. In particular, Syn II interacts directly with P/Q-type and indirectly with N-type Ca^{2+} channels to increase asynchronous release. Additionnally, Syn I(II) seem to constitute a push-pull mechanism regulating the ratio between synchronous and asynchronous release (*12*), thus suggesting a single exocytosis mechanism. The proposed model explains this by the timescale separation ε between p_1 and p_2. Deeper insight into this mechanism could result from further molecular studies investigating the existence of a signalling pathway between CB1 receptor and Syn I(II), since CB1 also appears to interact with N-type and P/Q-type Ca^{2+} channels (*23, 24*). Nevertheless, one should not rule out multiple exocytotic mechanisms. For instance, augmenting the model so as to discriminate, via new variables, between the different modes of exocytosis and allow for switches between them, is possible. It would be valuable to test this alternative model against recent data suggesting that intense stimulation forms a distinct, VAMP4-enriched, vesicle pool (from plasma membrane), which in turn preferentially fuses asynchronously (*6*). Surprisingly, the authors show that VAMP4-driven SNARE complexes do not readily interact with synap-

totagmin and complexin, which challenges the growing view that synchronous release requires interaction of SNARE complexes (e.g. VAMP4-SNAP-25 and Syntaxin-1) with molecules such as synaptotagmin 1 and complexins. This issue could be resolved by seeking an alternative way to elicit VAMP4-mediated release (identifying a different signalling pathway) and the VAMT-g model could be part of a modelling study accompanying such experiments. In light of the present manuscript's results, it would be relevant to determine such a pathway by testing for VAMP4 in synapses expressing CCK. Despite these observations, note that the VA-model can mimic this scenario, however without considering the formation of a second (VAMP4-enriched) pool of vesicles; see Fig. S6.

Model refinements will be explored as new data emerge. An immediate exploration will be based on a recent study showing that 2-AG/anandamide directly modulate $GABA_A$ post-synaptic receptors, therefore affecting neurotransmitter docking times and possibly contributing to asynchronicity (*28*). While the degradation of 2-AG has recently been explained (*29*), its synthesis is not fully understood. Nevertheless, modelling efforts should focus on a complete understanding of post-synaptic to pre-synaptic feedback (possibly with astrocytotic influence) that would inform experiments, before exploring network simulations. However, refinements of the proposed framework will facilitate large-scale network simulations, allowing to hypothesise the functional role of differential exocytosis and STSP on network states and how these relate to memory, cognition and pathological oscillations (e.g. epilepsy).

References and Notes

1. A. B. Ali, *J. Neurophysiol.* **98**, 861 (2007).

2. A. B. Ali, M. Todorova, *Eur. J. Neurosci.* **31**, 1196 (2010).

3. Z. P. Pang, T. C. Südhof, *Curr. Opin. Cell. Biol.* **22**, 496 (2010).

4. S. M. Smith, *et al.*, *Cell Calcium* (2012).

5. J. Yao, J. D. Gaffaney, S. E. Kwon, E. R. Chapman, *Cell* **147**, 666 (2011).

6. J. Raingo, *et al.*, *Nat. Neurosci.* **15**, 738 (2012).

7. V. Volman, R. C. Gerkin, P.-M. Lau, E. Ben-Jacob, G.-Q. Bi, *Phys. Biol.* **4**, 91 (2007).

8. S. Nadkarni, T. M. Bartol, T. J. Sejnowski, H. Levine, *PLoS Comput. Biol.* **6(11)**, 1 (2012).

9. V. Volman, H. Levine, T. J. Sejnowski, *PLoS Comput. Biol.* **6**, e1000973 (2010).

10. R. S. Zucker, *Neuron* **45**, 482 (2005).

11. E. Neher, T. Sakaba, *Neuron* **59**, 861 (2008).

12. L. Medrihan, *et al.*, *Nature Communications* **4**, 1 (2013).

13. Z. P. Pang, *et al.*, *Neuron* **70**, 244 (2011).

14. A. J. Groffen, *et al.*, *Science* **327**, 1614 (2010).

15. M. Desroches, M. Krupa, S. Rodrigues, *J. Math. Biol.* (2012). In press.

16. M. Krupa, P. Szmolyan, *Nonlinearity* **14**, 1473 (2001).

17. H. Markram, Y. Wang, M. Tsodyks, *Proc. Natl. Acad. Sci. USA* **95**, 5323 (1998).

18. Y. Wang, *et al.*, *Nat. Neurosci.* **9**, 534 (2006).

19. S. Raghavachari, J. E. Lisman, *J. Neurophysiol.* **92**, 2456 (2004).

20. J. S. Coggan, *et al.*, *Science* **309**, 446 (2005).

21. L. Danglot, T. Galli, *Biol. Cell* **99**, 349 (2007).

22. R. A. Lenz, J. J. Wagner, B. E. Alger, *J. Physiol.* **512.1**, 61 (1998).

23. W. Twitchell, S. Brown, K. Mackie, *J. Neurophysiol.* **78**, 43 (1997).

24. A. B. Ali, *J. Neurophysiol.* **105**, 1051 (2011).

25. C. A. C. del Rio, J. J. Lawrence, F. Erdelyi, G. Szabo, C. J. McBain, *J. Physiol.* **589.3**, 609 (2011).

26. L. Tricoire, *et al.*, *J. Neurosci.* **31(30)**, 10948 (2011).

27. F. Campillo, C. Lobry, *Ecol. Model.* **246**, 1 (2012).

28. E. Sigela, *et al.*, *Proc. Natl. Acad. Sci. USA* **108(44)**, 18150 (2011).

29. A. Tanimura, *et al.*, *Proc. Natl. Acad. Sci. USA* **109(30)**, 12195 (2012).

Supporting Online Material

www.sciencemag.org

Material and Methods

References *(30–39)*

Tables S1 and S2

Figs. S1 to S6

Figure legends

Fig.1 : (A) CCK-positive interneuron synaptic communication. A spike stimulus induces calcium influx and retrograde messenger, 2-AG or anandamide, binds to CB1, which triggers a signalling pathway that underlies delayed irregular release. The *sand watch* attempts to convey a delayed process upon inputs (2AG/anandamide, Ca^{2+} and spike-stimulus) in the VA-model. The output of the VA-model feeds into the MT-model and thus modulates the quantity of vesicles. $GABA_A$ is released and activates post-synaptic receptors. (B) VA-model (red), MT-model (blue), $GABA_A$ induced current and voltage (black) equations.

Fig.2 : (A) Interaction between protein complexes p_1 and p_2 along the vesicle cycle are given by the parabola and the horizontal line (black). These give rise to special points S, U, TC and SN, which mediate all the functions associated with the exocytotic-endocytotic cycle (red curve): Priming (P), Fusion (F), Endocytosis (E) and Refilling (R). (B1 and B2) Same information in the time domain. (B3) Analogy where spikes are required to activate the interaction between p_1 and p_2, represented as a particle that initiates movement only if sufficient energy is provided to traverse the energy barrier (U).

Fig.3 : (A) Synchronous mode: the input stimuli (square wave) elicits an immediate response in p_2 (units are adimensional); the delay is made arbitrarily small. (B) Delayed release upon a single input spike: delay arbitrarily large. (C) VA-model's sensitivity to initial conditions: irregular activation. The same input stimuli is provided and minor variations to the initial conditions give rise to different delayed outputs (cyan, red and magenta curves). (D) Delayed release upon a burst of spikes. The output signal can have variable rise and decay times upon modulation of system parameters. (E) Spontaneous release mode, excitable regime: small-amplitude noise is sufficient to trigger exocytosis. (F) Spontaneous release, limit cycle regime: noise in the limit cycle parameters enable irregular oscillations.

Fig.4 : Three types of unitary synaptic connections obtained by dual whole-recordings and spontaneous IPSPs are shown in the CA1 region of rat hippocampus. Single sweep raw data are superimposed and average responses are shown in bold traces. (A) Inhibitory connection between Schaffer collateral associated (SCA) to other SCA interneurons displays, synaptic facilitation. (B) Unitary connections between lacunosum moleculare, radiatum, perforant pathway (LM-R PP) to SCA connections display a delayed onset of release and average IPSPs display a slow time courses. (C) Connections between back-projecting interneurons in stratum radiatum to lacunosum moleculare perforant path (LM PP), display brief train depression, typically observed at inhibitory synapses. Facilitating synapses in (A) and (B) involve presynaptic cells that are immunoreactive for the neuropeptide CCK, that co-localise CB1 receptors. (D) Show by whole-cell recordings, most of these inhibitory interneurons receive spontaneous IPSPs.

Fig.5 : (A1) Delayed IPSP ($\sim$5.6ms) of CKK-positive SCA interneuron to unitary input spike at time t_{sp} (dashed-red line). (B1) The model with data. (A2) Depressed and delayed IPSP data resulting from spikes occurring at times t_{sp_i}, $i = \{1 \dots 5\}$ (red-dashed lines). First epoch (shaded magenta rectangle) is triggered by the first three spikes causing synchronous mode (release within 5ms); second epoch (shaded cyan rectangle) is initiated by two subsequent spikes that lead to asynchronous mode (at least 5ms delayed release). Inset: zoom into the region corresponding to the five release events; vertical red-dashed lines mark spike time-instants, vertical blue lines mark IPSP response times. The distance between them measures the delay: $\sim$(2;2.6;2.5;9.2;15)ms. (B2) Good agreement between model and data. (A3) Facilitated and delayed IPSP data. First epoch (shaded magenta rectangle), induced by the first three spikes, leads to synchronous release; response times $\sim$(4.2;3.6;4.1)ms. The second epoch (shaded cyan rectangle), evoked by two subsequent spikes, possesses marginal delayed release times ($\sim$(5;5.1)ms). (B3) Model agrees with data.

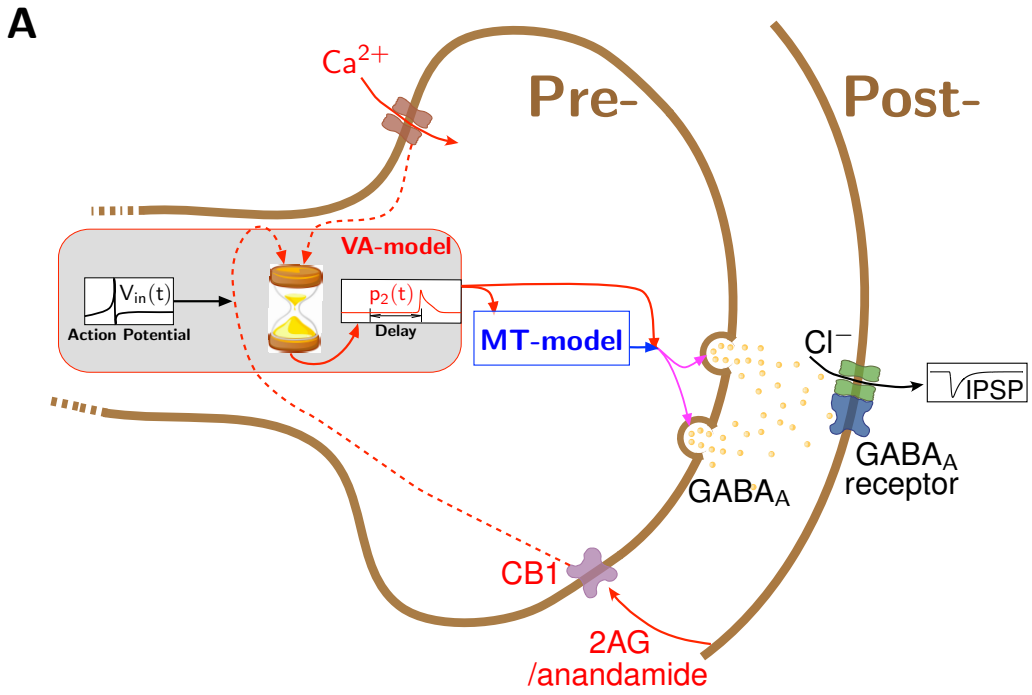

B

Pre-

$$\dot{p}_1(t) = \left[p_2(t) - (a p_1(t) + b)\right]\left[p_2(t) - (\tilde{a} p_1(t) + \tilde{b})\right](\alpha - p_2(t)) + V_{in}(t)$$

$$\varepsilon\, \dot{p}_2(t) = p_2(t)\left[p_1(t) - \left(\varkappa_2 p_2(t)^2 + \varkappa_1 p_2(t) + \varkappa_0\right)\right]$$

$$\dot{d}(t) = (1 - d(t))/\tau_D - d(t) f(t) p_2(t)$$

$$\dot{f}(t) = (f_0 - f(t))/\tau_F + F(1 - f(t)) p_2(t)$$

Post-

$$\dot{g}_{gaba}(t) = -g_{gaba}(t)/\tau_{gaba} + \bar{g}_{gaba}\, d(t) f(t) p_2(t)$$

$$C\, \dot{v}(t) = -g_L(v(t) - E_L) - g_{gaba}(t)(v(t) - E_{gaba})$$

Figure 1:

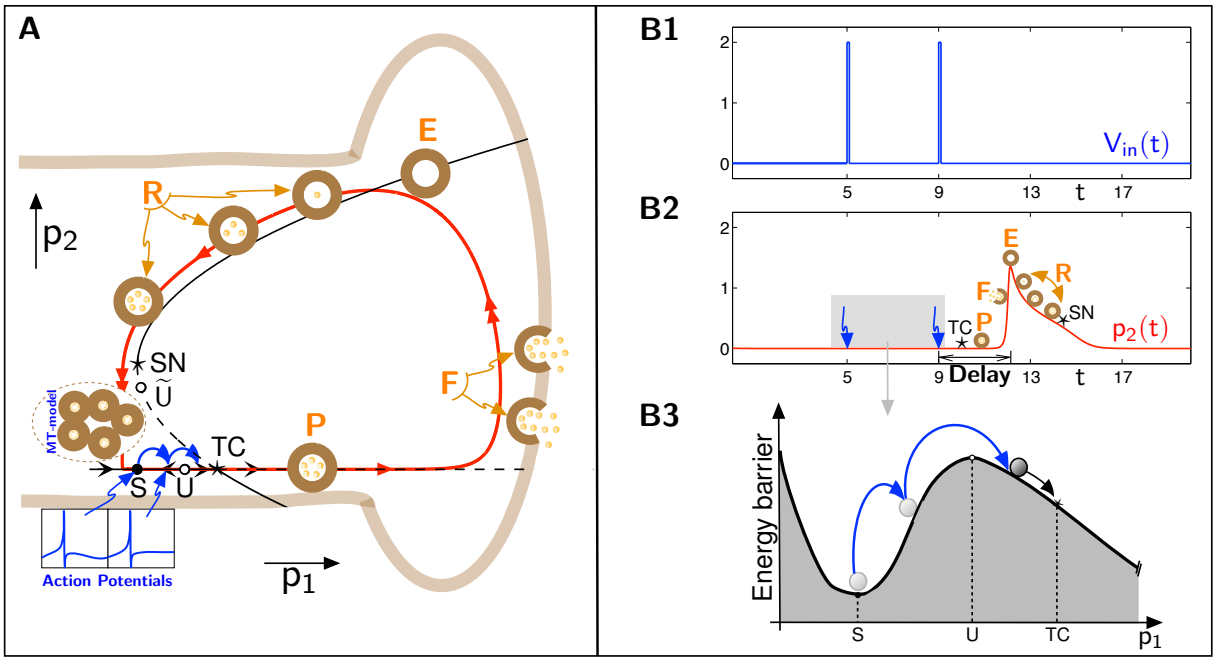
A
E
R
p2
SN
Ũ
F
MT-model
P
TC
S
U
Action Potentials
p1
B1
2
1
0
Vin(t)
5
9
13
t
17
B2
E
R
F
P
TC
SN
p2(t)
Delay
B3
Energy barrier
S
U
TC
p1

Figure 2:

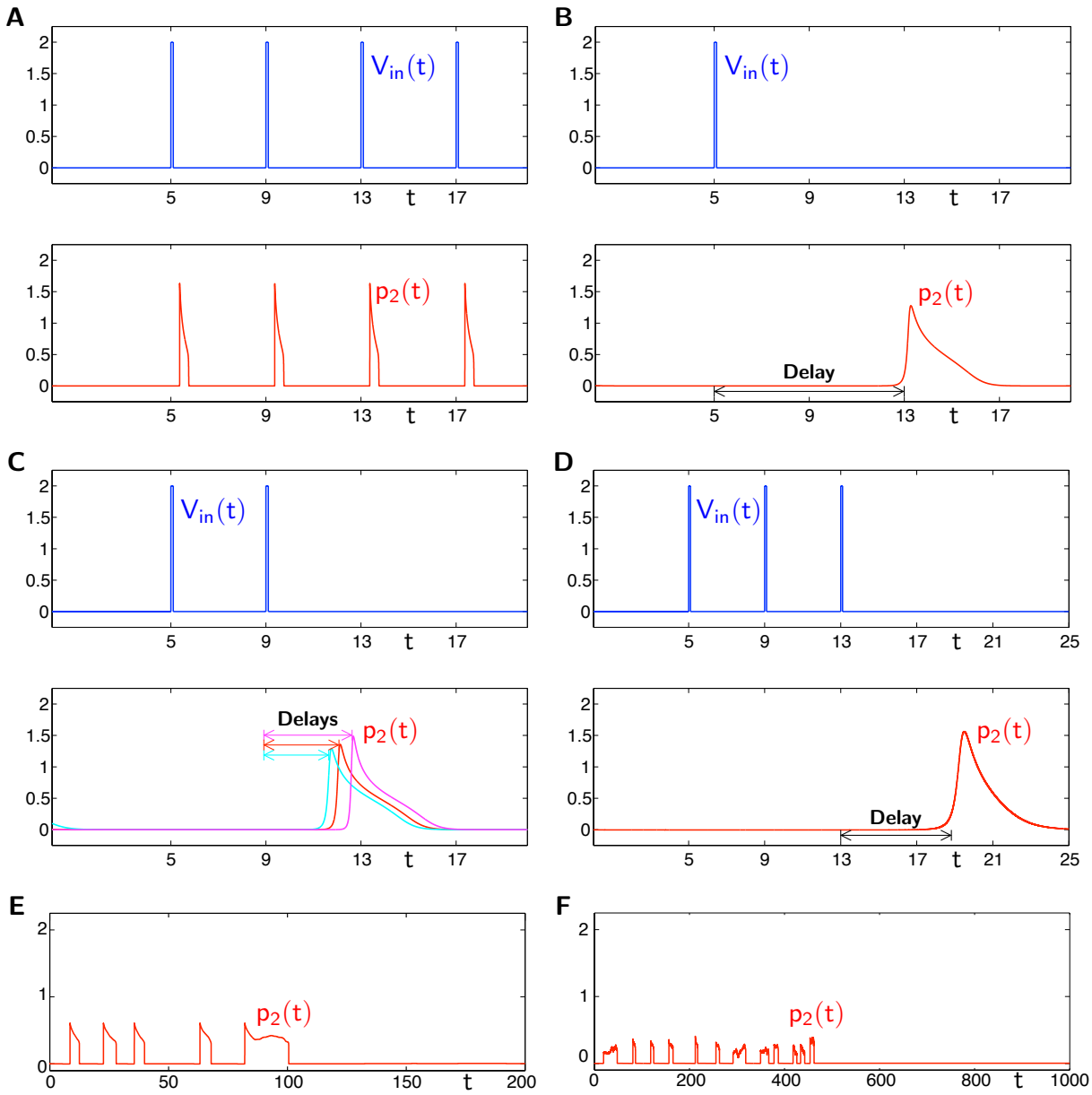

Figure 3:

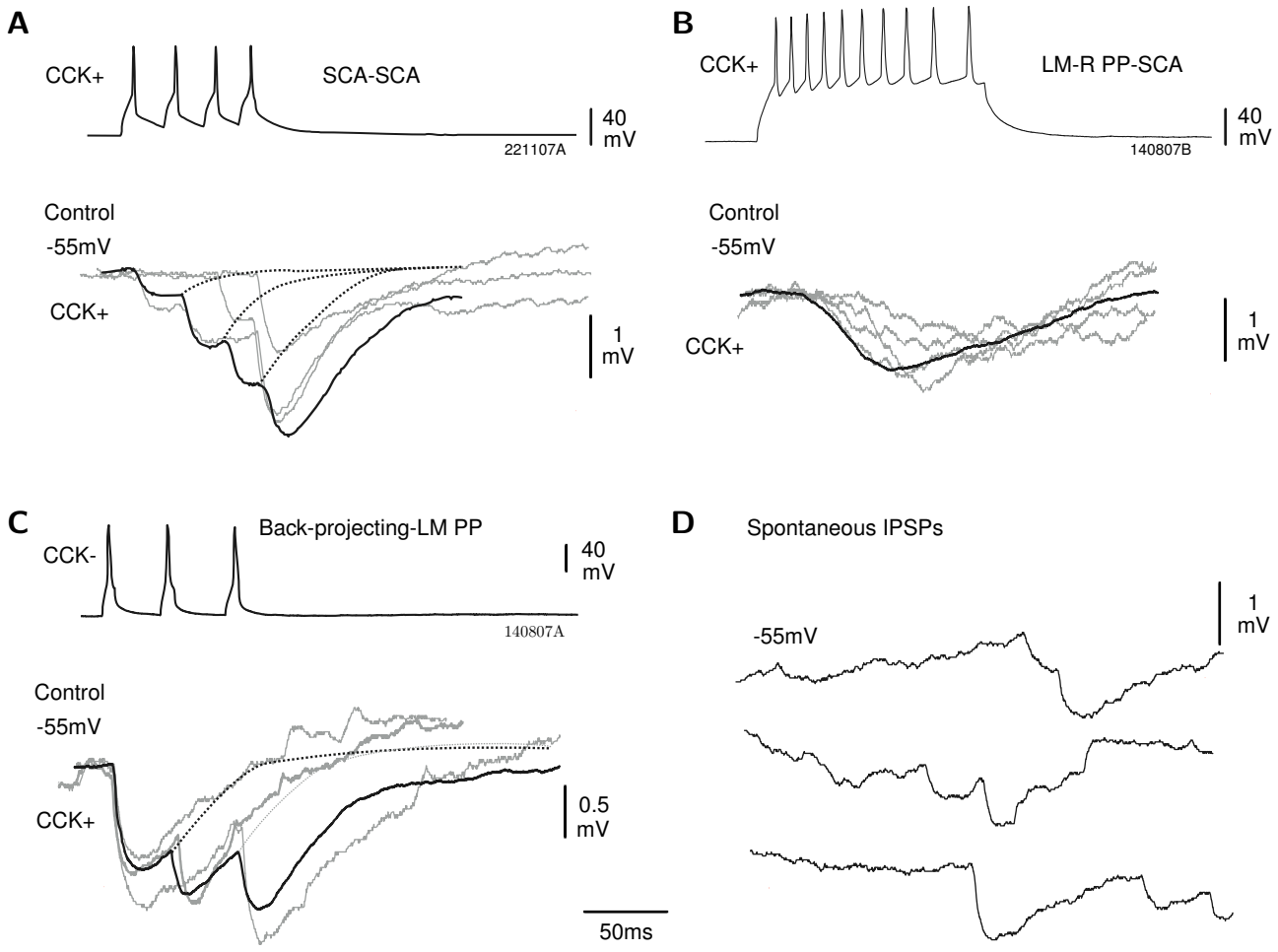
A
CCK+
SCA-SCA
40
mV
221107A
Control
-55mV
CCK+
1
mV
B
CCK+
LM-R PP-SCA
40
mV
140807B
Control
-55mV
CCK+
1
mV
C
CCK-
Back-projecting-LM PP
40
mV
140807A
Control
-55mV
CCK+
0.5
mV
50ms
D
Spontaneous IPSPs
1
mV
-55mV

Figure 4:

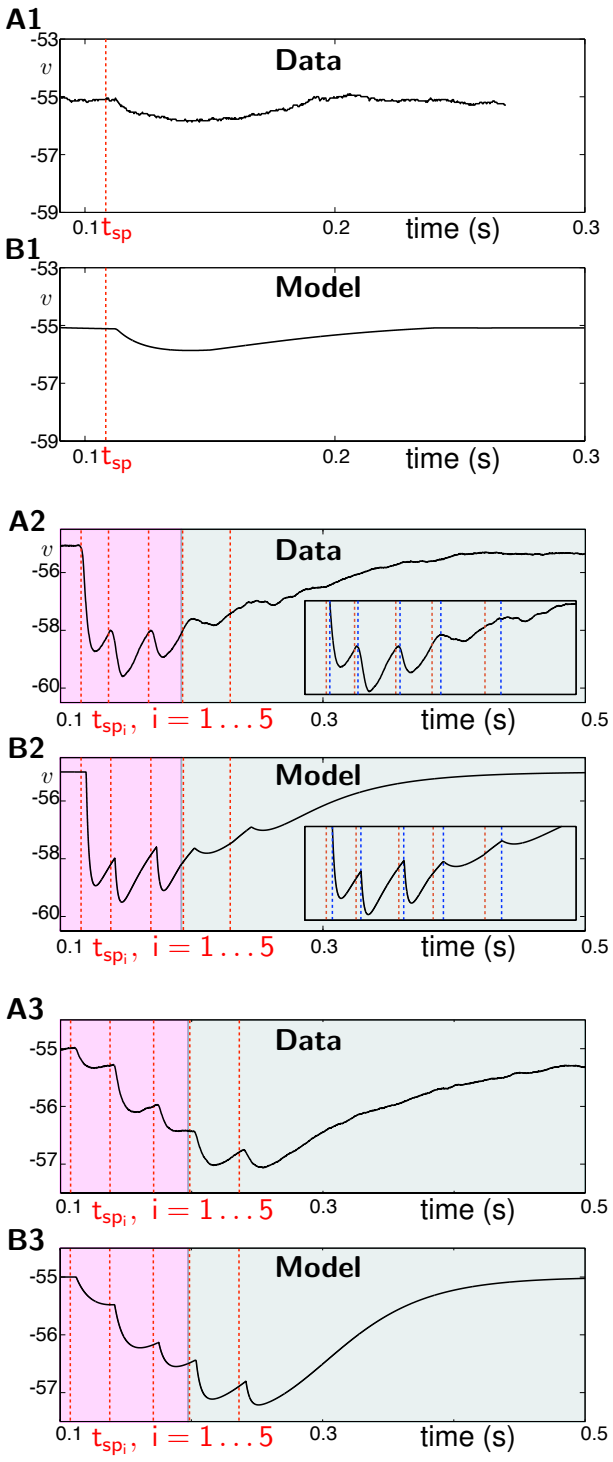
A1
Data
v
-53
-55
-57
-59
0.1
t_{sp}
0.2
time (s)
0.3
B1
Model
A2
Data
-56
-58
-60
t_{sp_i}, i = 1 . . . 5
0.5
B2
Model
A3
Data
B3
Model

Figure 5:

Supporting Online Material

Material and Methods

Softwares. Electrophysiological data were acquired and analysed off line using Signal from Cambridge Electronic Design, UK (CED). For model simulations, the commercial software package (MATLAB R2010b, The MathWorks Inc.), XPPAUT *(30)* were used. The parameter fitting of the model from data was carried out with MATLAB.

Slice preparation. Male Wistar rats (P18 - P23, Harlan, UK) were anaesthetised with sodium pentobarbitone (60mg/kg Euthatal, Merial, UK) via intraperitoneal injection and perfused transcardially with ice-cold modified artificial cerebral spinal fluid (ACSF), containing (in mM): 15 D-glucose, 248 sucrose, 2.5 CaCl2, 3.3 KCl, 1.2MgCl2, 25.5 NaHCO3 and 1.4 NaH2PO4. Following decapitation, the brain was removed and 300μm thick coronal slices of cerebral cortex were cut. These procedures were performed under UK Home office guidelines by authorised Home office licence holders. The severity of the procedures was classed as moderate. The total number of rats used for this study was 61. Slices were incubated for 1 hour prior to recording, for which they were placed in a submerged chamber perfused with ACSF at a rate of 1-2 mLmin-1. ACSF contained (in mM): 20 D-glucose, 2 CaCl2, 2.5 KCl, 1 MgCl2, 121 NaCl, 26 NaHCO3, and 1.25 NaH2PO4 (equilibrated with 95% O2 and 5% CO2). All substances used to make ACSF solutions were obtained from VWR, UK (See *(2)*).

Electrophysiological recordings. Electrodes with resistances of 8-11MΩ were pulled from borosilicate glass and filled with an intracellular solution containing (in mM): 144 K-gluconate, 0.2 EGTA, 10 HEPES, 3 MgCl2 0.2 Na2-ATP, 0.2 Na2-GTP, and 0.02% w/v biocytin (pH 7.2 - 7.4, 300mOsm). Slices were viewed using video microscopy under near-differential interference contrast (DIC) illumination to enable cells to be chosen based upon the shape of their soma and dendritic projections. Neurons were further identified by their firing properties following a series of 500ms depolarizing current steps from +0.05nA to +0.15nA. Dual whole cell recordings were

performed in current clamp at room temperature in CA1 stratum radiatum and lacunosum moleculare border. Presynaptic action potentials were generated by a depolarizing current injection of varying length (5-10ms) to enable Inhibitory Post Synaptic Potentials (IPSPs) to be observed in response to single, double or trains of action potentials. Connections were tested in both directions for all pairs. Data were acquired with SEC 05L/H amplifiers (npi electronics, GmbH). Recordings were filtered at 2KHz, digitized at 5KHz using a CED 1401 interface and stored on a hard disk drive. Input resistances were continually monitored by injecting a small hyperpolarizing current injection at duration of 20ms at the start of each frame.

Pharmacology. The endogenous CB receptor agonist, anandamide (in water soluble emulsion) (14μM) was used. AM-251 (1-(2,4-dichlorophenyl)-5-(4-iodophenyl)-4-methyl-N-(1-piperidyl)pyrazole-3-carboxamid, Tocris, UK), a selective CB1 receptor inverse agonist was dissolved in DMSO, stored as stock at -20C and bath applied at 10M. AM251 is structurally very close to SR141716A, a cannabinoid receptor antagonist, but exhibits a higher binding affinity for the CB1 receptor with a Ki value of 7.5nM compound to SR141716A, which has a Ki value of 11.5nM.

Electrophysiological data analysis. Using Signal (CED), the electrophysiological characteristics of the recorded cells were measured from their voltage responses to 500ms current pulses between -0.2 and +0.1nA in amplitude. Postsynaptic events were either accepted for analysis or rejected. Individual sweeps were observed and either accepted, edited, or rejected according to the trigger points that would trigger measurements and averaging of the IPSPs during subsequent data analysis. Averaging of IPSPs was triggered from the rising phase of the presynaptic spike. Apparent failures of synaptic transmission were counted manually, IPSP amplitudes in the range of the synaptic noise were taken as failures. Selection and averaging of these apparent failures resulted in no measurable postsynaptic responses. Single sweep IPSP amplitudes were measured from the baseline to the peak of the IPSP and are displayed as ± SD. IPSP half width and the 10-90% rise time were obtained from averages created from 100-300 sweeps. IPSP latencies were manually measured as the time delay between presynaptic action poten-

tial peaks to the onset of the detectable IPSPs. The fluctuations in the IPSP latencies were quantified in non-overlapping time interval sets of 5 ms after each presynaptic action potential. Synchronous release was taken as release of neurotransmitter within [0-5)ms latencies, whereas asynchronous release was taken as the release of neurotransmitter falling within a time window of [5-15)ms latencies *(2)*. The synchronicity ratio was calculated as the ratio of synchronous release/asynchronous release (from data set of 100-300 sweeps).

VA-model. Using principles of slow-fast dynamical systems theory *(31,16,32)* and inspiring from the work of Rosenzweig and MacArthur *(33,34)*, we build up a model that displays *excitability*, *delayed responses to input stimuli* and *limit-cycle dynamics*. Our model allows to describe the interactions between protein complexes (p_1, p_2) that reciprocally cooperate to generate the functions associated with the excoytotic-endocytotic cycle. The equations underlying these interactions are given as follows:

$$\begin{aligned} \dot{p_1} &= (p_2(t) - (ap_1t) + b))(p_2(t) - (\tilde{a}p_1(t) + \tilde{b}))(\alpha - p_2(t)) + V_{in}(t) \\ \varepsilon\dot{p_2} &= p_2(t)\left(p_1(t) - (\varkappa_2 p_2(t)^2 + \varkappa_1 p_2(t) + \varkappa_0)\right), \end{aligned} \tag{1}$$

where the overdots represent time derivatives ($\frac{d}{dt}$). The positive small parameter $0 < \varepsilon \ll 1$, induces a separation of timescales; p_1 evolves on a much slower timescale than p_2. The remaining parameters determines the model's mode: *excitability*, *delayed response to input stimuli* or *limit-cycle dynamics* (this will become clear progressively). $V_{in}(t)$ corresponds to a pre-synaptic stimulus. The right hand side of system (1), provides the rules of interaction between the protein complexes (p_1, p_2). These interactions are best described (in mathematical terms) by plotting the components of the rules (technically, *nullclines*) in a two-dimensional space spanned by the actions of p_1 and p_2 (*phase-space*), as mapped out in Fig. S1. This is carried out by representing the stationary activity of the protein complexes, that is, when $\dot{p_1} = 0$ and $\dot{p_2} = 0$. For the fast variable p_2, this yields two connected components, one of the fast nullclines being the horizontal line $\Gamma_1 \equiv \{p_2 = 0\}$ and the second the parabola $\Gamma_2 \equiv \{\varkappa_2 p_2^2 + \varkappa_1 p_2 + \varkappa_0\}$. The pale blue shaded

rectangle in Fig. S1 indicates the region of negative values of p_2, which from a biological point of view is irrelevant and thus will not be considered for the model dynamics. The half-lines and half-parabola (dashed) indicate regions of unstable stationary activity. The SN (*saddle-node equilibrium bifurcation*) is a special configuration point that connects the stationary stable (black upper half-parabola) and the stationary unstable activities (dashed half-parabola). This transition is where p_2 switches its stability and the associated point is neutral (neither stable nor unstable). Similarly, the slow nullclines are composed by three straight lines, namely Π_1, Π_2 and Π_3. The relative configurations between the involved nullclines define different regions in which the interaction between the protein complexes change (hence the joint rules are nonlinear).

The fast and slow nullclines intersect in three different points, namely S (*stable*), U (*unstable of saddle type*) and $\widetilde{\mathrm{U}}$ (*unstable*), corresponding to three (coexisting) equilibrium solutions of the system, for a given set of parameter values. Note, the condition $b \leq \tilde{\mathrm{b}}$ is the only case considered herein, since this renders S stable and U unstable. Also, the condition (α<-$\varkappa_1/(2\varkappa_2)$) is used, which makes $\widetilde{\mathrm{U}}$ unstable and does not affect the overall dynamics of the system. However , when α is close to the y-coordinate of the SN point then special limiting cases emerge (see section **VA-model exceptional cases**). Π_3 divides the space into two regions, which dictates how p_1 evolves. Specifically, below Π_3 the complex p_1 evolves towards the right (i.e. its activity increases), except in the region in-between S and U, where the basin of attraction of S forces it towards inactivity. In contrast, above Π_3 the activity of p_1 decreases (see the black arrows on Γ_1 and Γ_2). The vertical line F (brown) and its corresponding arrows indicate the direction in which the fast complex p_2 evolves. This is applicable everywhere except in the outer region of the dashed parabola segment, where p_2 evolves towards Γ_1. A special feature of the present model is that the fast nullclines Γ_1 and Γ_2 intersect at a *transcritical bifurcation* point TC (with coordinates $(\varkappa_0, 0)$), which characterises the exchange of stability seen simultaneously in Γ_1 and Γ_2 (transition from dashed to black lines). Note that SN and TC are configuration points of the fast system, however, their presence is felt, so to speak, as a 'ghost' configuration in the

full system (1), when the protein complexes interact. In particular, as the trajectory of the full system flows along Γ_1 towards increasing activity of p_1, it actually does not pass directly through the TC point. Rather it flows in the vicinity of TC (within an ε vertical distance from TC); denote this coordinate passage point $(p_{1,T}, 0)$ as illustrated in Fig. S2 (C) (zoom of the grey shaded rectangle of Fig. S2 (A)).

VA-model evoked release mode. This section examines evoked release (synchronous and asynchronous modes) in terms of phase-diagrams (Fig. S2 and Fig. S3), which complements the time series shown in Fig. 3 (main manuscript). For evoked release mode, system (1) is set to an *excitable regime*, which corresponds to setting $b = a(\varkappa_1^2/(4\varkappa_2) - \varkappa_0)$. This effectively aligns the S and SN points vertically (i.e. the coordinates of S are $(\varkappa_0 - \varkappa_1^2/(4\varkappa_2), 0)$). A sufficiently large amplitude of $V_{in}(t)$, or a sequence of input spikes, enables the system to escape the basin of attraction of the stable state S and go past the unstable point U. The system's activity flows along Γ_1 (specifically, an ε vertical distance away) towards increasing p_1, and past the $(p_{1,T}, 0)$ point as illustrated in Fig. S2 (C) (zoom of the grey shaded rectangle of Fig. S2 (A)). Slow-fast theory of *dynamic transcritical bifurcations (31,16,32)* ensures that the system's activity will flow in the vicinity of Γ_1, which past the TC point is repelling/unstable in the normal direction towards the upper segment of Γ_2. However, inertia will keep the activity along Γ_1. The associated trajectories are examples of *canards orbits (35,16)*. Specifically, *canards* are trajectories that contain segments following both attracting and repelling slow manifolds (in this case corresponding respectively to the half-left and half-right lines of Γ_1). Thus, the slow processes (seen as slowly-varying parameters) entrain the fast processes inducing delays and variabilities, which leads to sensitivity to initial conditions. This phenomenon is well known in the mathematical theory of slow-fast dynamical systems *(31,16,32)* and also observed experimentally (e.g. *(36)*). As the inertia slowly vanishes, this prompts a sudden jump of the trajectory towards the upper branch of Γ_2. However, as the flow traverses Π_3 it triggers the deactivation of p_1. The arrival of the flow onto Γ_2 also triggers the deactivation of p_2. Consequently, both p_1 and p_2 down regulate

their activity, passing via the SN point and finally become inactive (S). The delayed response of the system to an input is entirely governed by the nullclines of the fast system and by the so-called *way-in-way-out function* (see next section), which measures the balance between the contraction rate (attraction or binding) towards Γ_1 (to the left of TC) and subsequent expansion rate (repelling or un-binding) away from Γ_1 (towards the right of TC). Therefore, this allows full control of the delay by suitably tuning system parameters, in particular ε, as well as initial conditions. Consequently, synchronous and asynchronous response regimes result upon a minor parameter change (see Table S1, 2nd-3rd columns). The information presented in Fig. S2 complements Fig. 3 (C) (main manuscript), where the phase-diagram (Fig. S2 (A)) illustrates the associated trajectories in phase-space; Fig. S2 is a replica of Fig. 3 (C) (main manuscript). A change in initial conditions shows variability in the delayed response, which in this case varies between 8 to 12 time units; compare the magenta, red and cyan responses in panel (B2) for the same input signal from panel (B1). The synchronous mode is shown in Fig. S3 (phase-diagram), which complements the time-series of Fig. 3 (A) (main manuscript). Here, the time scale separation between the protein complexes is reduced, which induce output responses occurring within one time unit.

VA-model spontaneous release mode. This section examines the two modes of spontaneous release in terms of phase diagrams. Similarly to the evoked release mode, the first form of spontaneous release is set by placing the system into an *excitable regime*, see Table S1 (4th column). However, the distance between S and U points is small enough so that a small noise perturbation is sufficient to trigger an exocytotic-endocytotic cycle; compare phase-diagram in Fig. S4 (A1) and time-series in Fig. S4 (B1) or Fig. 3 (E) (main manuscript). In particular, a noise term is added in the p_1-direction enabling the activity to escape the basin of attraction of the stable state S thus leading to an exocytotic-endocytotic cycle. The alternative spontaneous release mode is set by placing the system in a *limit-cycle* regime, see Table S1 (5th column). The self-sustained oscillation is triggered by moving S and U to the left (along Γ_1) so that none

of them is vertically aligned with the SN point. This is illustrated by phase-diagram Fig. S4 (A2), which complements the time series of Fig. S4 (B2) or Fig. 3 (F) (main manuscript). The oscillations can be made irregular by modulating the position of Γ_2, for instance, by perturbing it with noise. Note that in both forms of spontaneous activations, the width of Γ_2 is made small in order to relate to the *kiss-and-run* endocytosis that mediates release of neurotransmitters in small quantities.

VA-model's way-in-way-out function. A delay induced by a dynamic bifurcation can be estimated by the so-called entry/exit or *way-in-way-out function*; see *(16)* for details. For completeness, a brief description of its formulation is provided. As discussed, the VA-model (1) possesses a family of quasi-stationary points along Γ_1 with a dynamic transcritical bifurcation TC at $(p_{1,T}, 0)$ where $p_{1,T} = \varkappa_0$ (see Fig. S2 (C), shaded region). Thus every initial condition $(p_{1,0}, p_{2,0})$, taken in the vicinity of Γ_1 with $p_{1,0} < p_{1,T}$ results in a trajectory that is quickly attracted to an ε-neighbourhood of Γ_1 and towards increasing p_1 activity. The trajectory flow passes through $p_{1,T}$ and continues to follow the (now repelling) horizontal axis until it gets repelled away in exit point $p_{1,ex}$. The exit point is determined as a function of the entry point. This functional relationship can be established equivalently in terms of exit and entry times, since along Γ_1 the slow variable p_1 is a simple drift and thus behaves like time. Given a system in the following general form (satisfied by the VA-model (1)),

$$\dot{p_1} = F(p_1, p_2) \tag{2}$$

$$\varepsilon\dot{p_2} = G(p_1, p_2), \tag{3}$$

then the exit time t_{ex} is defined uniquely via the following entry/exit condition

$$\int_0^{t_{ex}} G_{p_2}(p(t))dt = 0. \tag{4}$$

Here G_{p_2} is the derivative of G with respect to p_2 and $p(t) = (p_1(t), 0)$, where $p_1(t)$ is the

solution of the slow system $\dot{p_1} = F(p_1, 0)$ with initial condition $p_{1,0}$. For the VA-model, the slow subsystem is, $\dot{p_1} = \alpha(ap+b)(\tilde{a}p+\tilde{b}) \equiv R_2p^2 + R_1p + R_0$, which corresponds to a Riccati equation with constant coefficients, therefore a separable equation that can be explicitly solved for any triple (R_0, R_1, R_2) using the equality

$$\int \frac{dp_1}{R_2p_1^2 + R_1p_1 + R_0} \quad = \quad \int dt. \tag{5}$$

Consequently, assuming only the presence of the transcritical bifurcation point, the entry/exit formula is explicit for the VA-model. However, in the VA-model the dynamics resulting from the presence of the unstable point U introduces a small bias in the estimation of the delay and the exact exit point. This estimation error is not critical for the present study. The precise estimation is beyond the scope of the present work and will be matter of future considerations since the complete *way-in-way-out function* will encode all the information about delayed release.

VA-model exceptional cases. Exceptional solutions of the VA-model are subsequently discussed. These limit case solutions are very sensitive to perturbations, so that numerical integration may be insufficient to compute them; moreover, some of them are unstable. A reliable method to compute them is the so-called *pseudo-arclength numerical continuation methods* provided by, e.g., the software package XPPAUT *(30)*. From a biological viewpoint these are extremely rare events, nevertheless, for completeness they are herein described. The exceptional regimes correspond to having the slow nullcline Π_3 intersect Γ_2 at an order-ε distance from the fold point (SN); see Fig. S1. Specifically, α must be ε-close to the value $-\varkappa_1/(2\varkappa_2)$ and it can only vary by an exponentially small quantity (in ε), showing that these solutions are not persistent. Nonetheless, this induces the so-called *fold-initiated canard cycles (35,37)*, which correspond to trajectories that do not immediately drop off the fold point, SN, but rather follow for some time the lower repelling branch of Γ_2. There exists a whole family of such canard cycles parameterised in this case by α. Three particular cases of such cycles are shown in Fig. S5 (compare the phase-diagrams and time series). The canard denoted C_h (red) is an example of

so-called *headless canard (35,37)*, where the trajectory flows along the repelling branch of Γ_2 and then jumps back to the attracting branch of Γ_2 (upper part of the parabola). In other words, C_h oscillates around the fold point SN and may represent vesicles escaping pathologically the release cycle; see panels (A) and (B1). The largest headless canard is called *maximal canard*, C_m *(35,37)*. This corresponds to a canard cycle following the repelling branch Γ_2 for the longest segment, that is, down to the transcritical point TC; see panels (A) and (B2). The remaining canard, denoted C_{wh}, as shown in panels (A) and (B3), is an example of so called *canard with head (35,37)*. Such a canard cycle owes its name to the fact that, in contrast to previous cases, it follows the repelling branch of Γ_2 and instead jumps towards Γ_1, giving rise to a cycle that changes its curvature. In this case, following the jump the trajectory passes ε-close to the transcritical point TC (more specifically $p_{1,T}$; see Fig. S2 (C)) and, hence, enters a delayed release cycle. The canard cycle repeats indefinitely, it is a stable *limit cycle*, and this could represent yet another form of spontaneous release but one in which at least one spike stimulus is required to initiate the process. The point in the vicinity of Γ_1 (an ε vertical-distance away) onto which the trajectory lands after leaving the repelling branch of Γ_2 determines the entry point of the *way-in-way-out function* and thus determines the duration of the delay. The closer this entry point is to the unstable point U, the longer the delay will be. In the limit, where the entry point aligns vertically with the U point, the trajectory will flow along the *stable manifold* of U (typically denoted as $W^s(\mathrm{U})$) and will take an infinite amount of time to converge to U. The critical value of α that leads to this scenario marks the mathematical boundary between periodic and non-periodic regimes. In particular, this critical α marks the termination of canard cycles but also the initiation of solutions that emerge from U and flow along Γ_1 towards increasing values of p_1 (i.e. the *unstable manifold* of U, typically denoted as $W^u(\mathrm{U})$). Therefore, the family of canard cycles terminate in a connection at infinity between the stable and unstable manifolds of U, that is, a *homoclinic bifurcation at infinity*. Beyond that critical value of α, the canard trajectories follow the repelling branch of Γ_2 past the SN point, jump and land in the vicinity (an ε vertical-distance away) of Γ_1 to the left of U, which results in a flow towards the stable

equilibrium point S. A further exceptional case worth noting is that, since Γ_1 is an invariant manifold (line) even for $\varepsilon > 0$, then an initial condition exactly on Γ_1 leads to a trajectory that stays on it for all future times, hence resulting in an unbounded delay. However, this case corresponds to a pathological scenario where the protein p_2 is 0 (i.e. vanishes). Finally, it is worth remarking that all the above cases are not robust to noise and thus are not representative of a typical exocytosis-endocytosis cycle.

VAMT-g model, simulations and data-fitting. The VA-model feeds its output signal, p_2, into the Markram-Tsodyks' (MT) model *(38,39,17)* as well as into the equations modelling GABA induced currents responsible for the activation of inhibitory post-synaptic potentials (IPSP). Consequently the VAMT-g model is composed by system (1) and the following set of equations:

$$\begin{aligned} \dot{d} &= (1-d)/\tau_D - dfp_2 \\ \dot{f} &= (f_0 - f)/\tau_F + F(1-f)p_2, \end{aligned} \tag{6}$$

representing the MT equations, and the dynamics of IPSP, described by the following conductance-based equations:

$$\begin{aligned} \dot{g}_{\text{gaba}} &= -g_{\text{gaba}}/\tau_{\text{gaba}} + \overline{g}_{\text{gaba}} dfp_2 \\ C\dot{v} &= -g_L(v - E_L) - g_{\text{gaba}}(v - E_{\text{gaba}}). \end{aligned} \tag{7}$$

The MT-model (6) is sometimes termed the *vesicle depletion model* as it describes the time evolution of finite resources (e.g. a vesicle pool). The synaptic resources (in the pre-synaptic terminal) can be in two states: *available* to be released or *non-available* for release. The overall fraction of available vesicles is $d(t)$ and the non-available vesicles is $1 - d(t)$. The activation of the exocytotic machinery mediated by the VA-model outputs signal p_2, which feeds into the MT-model, leading to consumption of resources. The consumption rate in the transition

from $d(t)$ to $1 - d(t)$ is proportional to $p_2(t)f(t)$, which leads to depression. The recovery from *non-available* to *available* states occurs at a rate $1/\tau_d$, where τ_d represents the spontaneous recovery time from the depressed state. The variable $f(t)$ controls the release probability of available neurotransmitters. The transition from *non-releasable* to *releasable* has rate $Fp_2(t)$, which describes activity-induced facilitation. The reversed transition occurs spontaneously at a rate $(f_0 - f)/\tau_f$, where f_0 is the baseline activity of $f(t)$. Parameters for the MT-model were adopted from *(38,39,17)*, however further parameter fitting from experimental data was performed (see Table S2). The voltage equation (7), represented by the variable $v(t)$, describes IPSP activations, which is induced by $GABA_A$ currents, $I_{\text{gaba}} = g_{\text{gaba}}(v - E_{\text{gaba}})$, where E_{gaba} is the $GABA_A$ reversal potential. The fist term of the right-hand side of the voltage equation represents the leaky current, g_L being the leaky conductance and E_L the leaky reversal potential. Parameter C represents the membrane capacitance. The $GABA_A$ conductance, g_{gaba} follows a first-order kinetic equation. Upon binding of neurotransmitters, the conductance increases by the amount $\overline{g}_{\text{gaba}} df p_2$, where $\overline{g}_{\text{gaba}}$ is the maximal $GABA_A$ conductance. The unbinding of neurotransmitters decreases the $GABA_A$ conductance, which occurs with a finite decay time τ_{gaba}. The parameters for equation (7) were extracted from *(1,25,26)*. Table S2 shows the parameter values (and their range) for parameter fitting of the VAMT-g model to experimental data.

References and Notes

1. A. B. Ali, *J. Neurophysiol.* **98**, 861 (2007).

2. A. B. Ali, M. Todorova, *Eur. J. Neurosci.* **31**, 1196 (2010).

3. Z. P. Pang, T. C. Südhof, *Curr. Opin. Cell. Biol.* **22**, 496 (2010).

4. S. M. Smith, *et al.*, *Cell Calcium* (2012).

5. J. Yao, J. D. Gaffaney, S. E. Kwon, E. R. Chapman, *Cell* **147**, 666 (2011).

6. J. Raingo, *et al.*, *Nat. Neurosci.* **15**, 738 (2012).

7. V. Volman, R. C. Gerkin, P.-M. Lau, E. Ben-Jacob, G.-Q. Bi, *Phys. Biol.* **4**, 91 (2007).

8. S. Nadkarni, T. M. Bartol, T. J. Sejnowski, H. Levine, *PLoS Comput. Biol.* **6(11)**, 1 (2012).

9. V. Volman, H. Levine, T. J. Sejnowski, *PLoS Comput. Biol.* **6**, e1000973 (2010).

10. R. S. Zucker, *Neuron* **45**, 482 (2005).

11. E. Neher, T. Sakaba, *Neuron* **59**, 861 (2008).

12. L. Medrihan, *et al.*, *Nature Communications* **4**, 1 (2013).

13. Z. P. Pang, *et al.*, *Neuron* **70**, 244 (2011).

14. A. J. Groffen, *et al.*, *Science* **327**, 1614 (2010).

15. M. Desroches, M. Krupa, S. Rodrigues, *J. Math. Biol.* (2012). In press.

16. M. Krupa, P. Szmolyan, *Nonlinearity* **14**, 1473 (2001).

17. H. Markram, Y. Wang, M. Tsodyks, *Proc. Natl. Acad. Sci. USA* **95**, 5323 (1998).

18. Y. Wang, *et al.*, *Nat. Neurosci.* **9**, 534 (2006).

19. S. Raghavachari, J. E. Lisman, *J. Neurophysiol.* **92**, 2456 (2004).

20. J. S. Coggan, *et al.*, *Science* **309**, 446 (2005).

21. L. Danglot, T. Galli, *Biol. Cell* **99**, 349 (2007).

22. R. A. Lenz, J. J. Wagner, B. E. Alger, *J. Physiol.* **512.1**, 61 (1998).

23. W. Twitchell, S. Brown, K. Mackie, *J. Neurophysiol.* **78**, 43 (1997).

24. A. B. Ali, *J. Neurophysiol.* **105**, 1051 (2011).

25. C. A. C. del Rio, J. J. Lawrence, F. Erdelyi, G. Szabo, C. J. McBain, *J. Physiol.* **589.3**, 609 (2011).

26. L. Tricoire, *et al.*, *J. Neurosci.* **31(30)**, 10948 (2011).

27. F. Campillo, C. Lobry, *Ecol. Model.* **246**, 1 (2012).

28. E. Sigela, *et al.*, *Proc. Natl. Acad. Sci. USA* **108(44)**, 18150 (2011).

29. A. Tanimura, *et al.*, *Proc. Natl. Acad. Sci. USA* **109(30)**, 12195 (2012).

30. B. Ermentrout, *Simulating, analyzing, and animating dynamical systems: a guide to XPPAUT for researchers and students*, vol. 14 (SIAM, 2002).

31. C. Lobry, *Dynamic Bifurcations*, E. Benoît, ed. (Springer, 1991), vol. 1493 of *Lecture Notes in Math.*, pp. 1–13.

32. H. Boudjellaba, T. Sari, *J. Differ. Equations* **246**, 2205 (2009).

33. M. L. Rosenzweig, R. H. MacArthur, *Amer. Nat.* pp. 209–223 (1963).

34. A. A. Pokrovskii, E. Shchepakina, V. Sobolev, *J. Phys.: Conf. Ser.* **138**, 012019 (2008).

35. E. Benoît, J.-L. Callot, F. Diener, M. Diener, *Coll. Math.* **32**, 37 (1981).

36. P. Strizhak, M. Menzinger, *J. Chem. Phys.* **105**, 10905 (1996).

37. M. Krupa, P. Szmolyan, *SIAM J. Math. Anal.* **33**, 286 (2001).

38. H. Markram, M. Tsodyks, *Nature* **382**, 807 (1996).

39. M. Tsodyks, H. Markram, *Proc. Natl. Acad. Sci. USA* **94**, 719 (1997).

Table legends

Table S1: Parameter values for the VA-model that allow to tune the model into the different regimes: *excitability*, *delayed responses* and *limit cycle*. The second column corresponds to synchronous release mode (excitability). The third column, asynchronous release mode (excitability and delayed response). The fourth column, spontaneous release mode via equilibria (excitability). The fifth column, spontaneous release model via limit cycle.

Table S2: Parameters for the VAMT-g model. Two different values in one entry box corresponds to fitting two different epochs within a given IPSP time series.

Parameters	**Synch. mode**	**Asynch. mode**	**Spont. mode (eq.)**	**Spont. mode (cycle)**
a	-1	-1	-1	-1
b	0.25	0.25	0.25	0.3
$\tilde{a}$	-1	-1	-1	-1
$\tilde{b}$	0.28	(0.28, 0.4)	0.5	0.35
α	0.4	0.4	(0.1, 0.2)	0.15
ε	(10^{-4}, 10^{-2})	(0.1, 0.5)	(10^{-4}, 10^{-2})	($10^{-4}, 10^{-2}$)
$\varkappa_0$	0.3	0.5	0.68	0.66
$\varkappa_1$	-0.2	-1	-1.8	(-2.5, -1.5)
$\varkappa_2$	0.2	1	3	5

Table S1:

Symbol	**Description**	**Fig. 5 B1**	**Fig. 5 B2**	**Fig. 5 B3**
$radius$	Patch radius of the electrode micro-pipet	0.2e-3cm		
$A = 4\Pi(radius)^2$	The membrane area covered by the electrode	[-]cm^2		
C	Membrane capacitance	196e-6 μF		
R	Leak membrane resistance	220 MΩ	260 MΩ	220 MΩ
$c_m = C/A$	Specific membrane capacitance	[-] μF/ cm^2		
$r_m = R * A$	Specific membrane resistance	$[-]M\Omega$ cm^2		
$\tau_m = C * R$	Membrane time constant	43.1 ms		
E_L	Leak reversal potential	-55mV	-55mV	-55mV
τ_{gaba}	Decay time constant of $GABA_A$	25ms	6ms / 17ms	20ms
E_{gaba}	Reversal potential for $GABA_A$	-57mV	-60mV	-57mV / -57.5mV
$\bar{g}_{gaba}$	Peak $GABA_A$ conductance	1 mS/cm^2	1 mS/m^2	1mS/m^2
τ_F	Recovery time of synaptic facilitation	150 ms	1500ms / 0.15ms	2500ms
τ_D	Recovery time of synaptic depression	0.2 ms	100ms	100ms
F	Resting release probability	0.001	1 / 0.0035	0.25 / 0.7

Table S2:

Figure legends

Fig. S1: Dynamics of the VA-model. The fast nullclines Γ_i, $i = 1, 2$ (corresponding to $\dot{p_2} = 0$) are shown in black. The slow nullclines Π_i, $i = 1, 2, 3$ (i.e. for $\dot{p_1} = 0$) are shown in grey. A representative fast fiber F, corresponding to the fast system, where p_1 is frozen and considered as a parameter, is shown in brown. The equilibria of the VA-model correspond geometrically to intersection points between a fast nullcline and a slow nullcline. The stable equilibrium, denoted S, is marked by a black dot. The unstable equilibria, U and $\widetilde{\text{U}}$, are marked by black circles. The bifurcation points of the fast system p_2 (with p_1 treated as a parameter) are indicated by stars : the saddle-node point SN and the transcritical point TC. The flow of the slow system is indicated by single black arrows on Γ_i, and the flow of the fast system is indicated by double brown arrows on F. The half-plane $\{p_2 < 0\}$ (pale blue shade) emphasizes that this region is irrelevant biologically as, in cases considered here, p_2 remains strictly positive in the VA-model.

Fig. S2: Asynchronous release in the VA-model. (A) Phase diagram showing the output of the model. (B1) The input stimuli. (B2) The same information as in panel (A), but now shown in time domain. The different trajectories (cyan, red and magenta) show sensitivity to initial conditions of the delayed responses. Panel (C) zooms in the grey rectangle of panel (A) and illustrates of the *way-in-way-out function* which organises the delay to the transcritical bifurcation $p_{1,T}$, from the entry point $p_{1,0}$ to the exit point $p_{1,ex}$. The sand-watch-like brown shaded area emphasises that trajectories are attracted towards Γ_1 and after the delayed transcritical bifurcation they are repelled away. For parameter values, see the third column of Table S1.

Fig. S3: Synchronous release in the VA-model. (A) Phase diagram showing the output of the model. (B1) The input stimuli. (B2) The same information as in panel (A), but now shown in time domain. For parameter values, see the second column of Table S1.

Fig. S4: Spontaneous release in the VA-model. (A1) Spontaneous release via excitability regime shown in the phase space (model output in red). Here S and U are placed close to each other and the amplitude of Γ_2 is decreased. Noise is added in the p_1-direction, which allows the

flow to escape the basin of attraction of the stable equilibria S. (B1) The same information as in panel (A1), but now shown in time domain. (B1) Spontaneous release via a limit cycle regime shown in phase space (model output in red). Here S and U are placed to the left of Γ_1 leading to a non vertical alignment with the SN point, which results into a limit cycle. The limit cycle is made irregular by adding small noise to Γ_2. (B2) The same information as in panel (A2), but now shown in time domain. For parameter values, see the fourth and fifth columns of Table S1, respectively.

Fig. S5: (A) Shows exceptional trajectories, namely *canard cycles* (*?*), of the VA-model in phase diagram. These cycles follow the repelling branch of Γ_2 (past the saddle node point SN) for an order-1 length. Three different cases are shown. First case: a *headless canard*, C_h (red) completes its cycle by following a fast segment upwards back to the attracting branch of Γ_2. Second case: the largest *headless canard*, called *maximal canard*, C_m (blue), flows maximally until it reaches the transcritical TC point. Third case: a *canard with head*, C_{wh} (green) which, in contrast to the other cases, follows the repelling branch of Γ_2 and then jumps towards Γ_1 (i.e. changes its local curvature). (B1) Shows C_h in the time domain. (B2) Shows C_m in the time domain. (B3) Shows C_{mh} in the time domain. For parameter values, refer to the third column of Table 1 except for α, which varies and allows to display the family of canard cycles. However, the variation in α is within an exponentially small interval so that, for the chosen value of ε, the 11 first decimal places of the values of α for C_h, C_m and C_{wh} are the same: 0.50025024345.

Fig. S6: The VA-model mimics VAMP4-mediated delayed release. (A) Phase-diagram shows that intense stimulation (shown by a sequence of curved blue arrows) first generates a synchronous release and subsequently a delayed release. Initially, the unstable equilibrium U is placed to the left (when compared to the projection of SN onto Γ_1). Also, S and U are sufficiently far apart so that only intense stimulation enables the activation of spontaneous release and subsequent delayed release (in fact with the possibility of multiple delayed releases as the system is now in a limit-cycle regime). Terminating the delayed release cycle requires moving the unstable point U to the right (point marked $U^\star$) to ensure that the endocytotic

activity falls into the basin of the attraction of S. Moving U to the right may represent the modelling of some physiological process that terminates the exocytotic-endocytotic cycle. (B1) The input stimuli. (B2) Depicts the same information as panel (A) but in the time domain. The parameter values for this case are the same as in the third column of Table S1 except for: $b = 0.05$, $\tilde{b} = 0.2$; for $U^{\star}$, the value of $\tilde{b}$ is increased to 0.28.

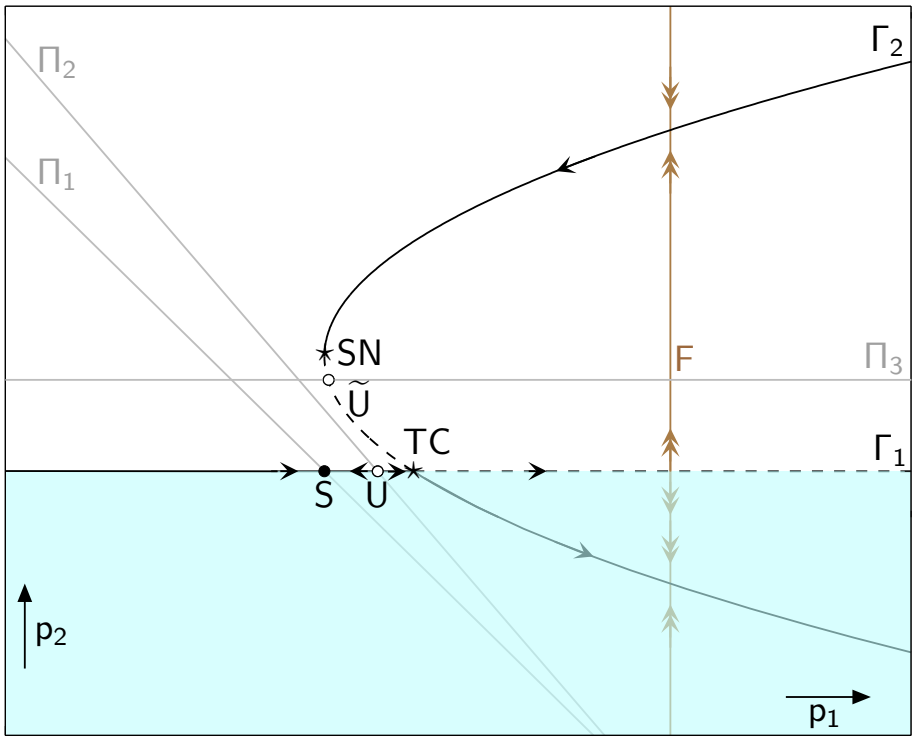

Figure S1:

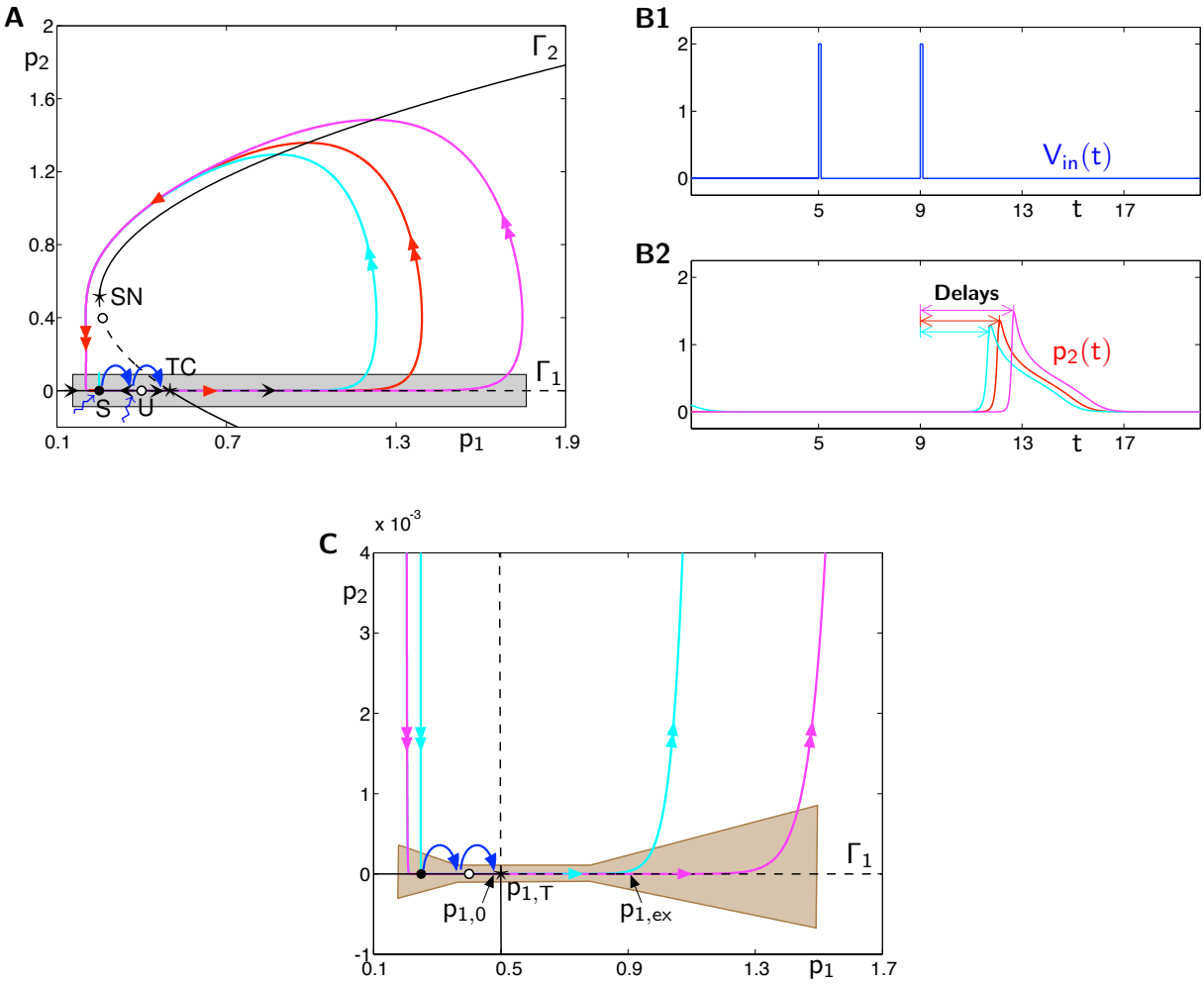

Figure S2:

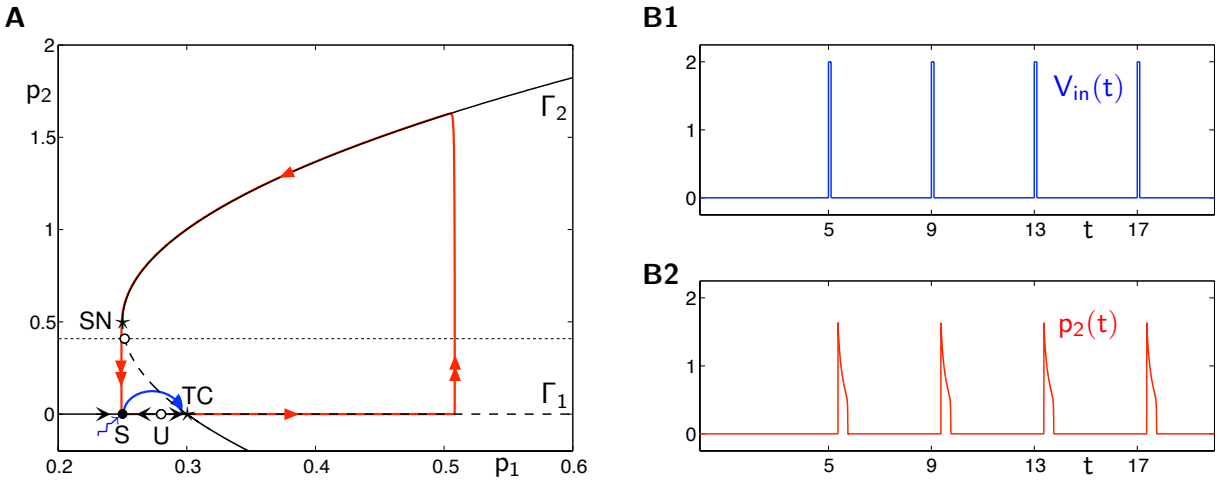

Figure S3:

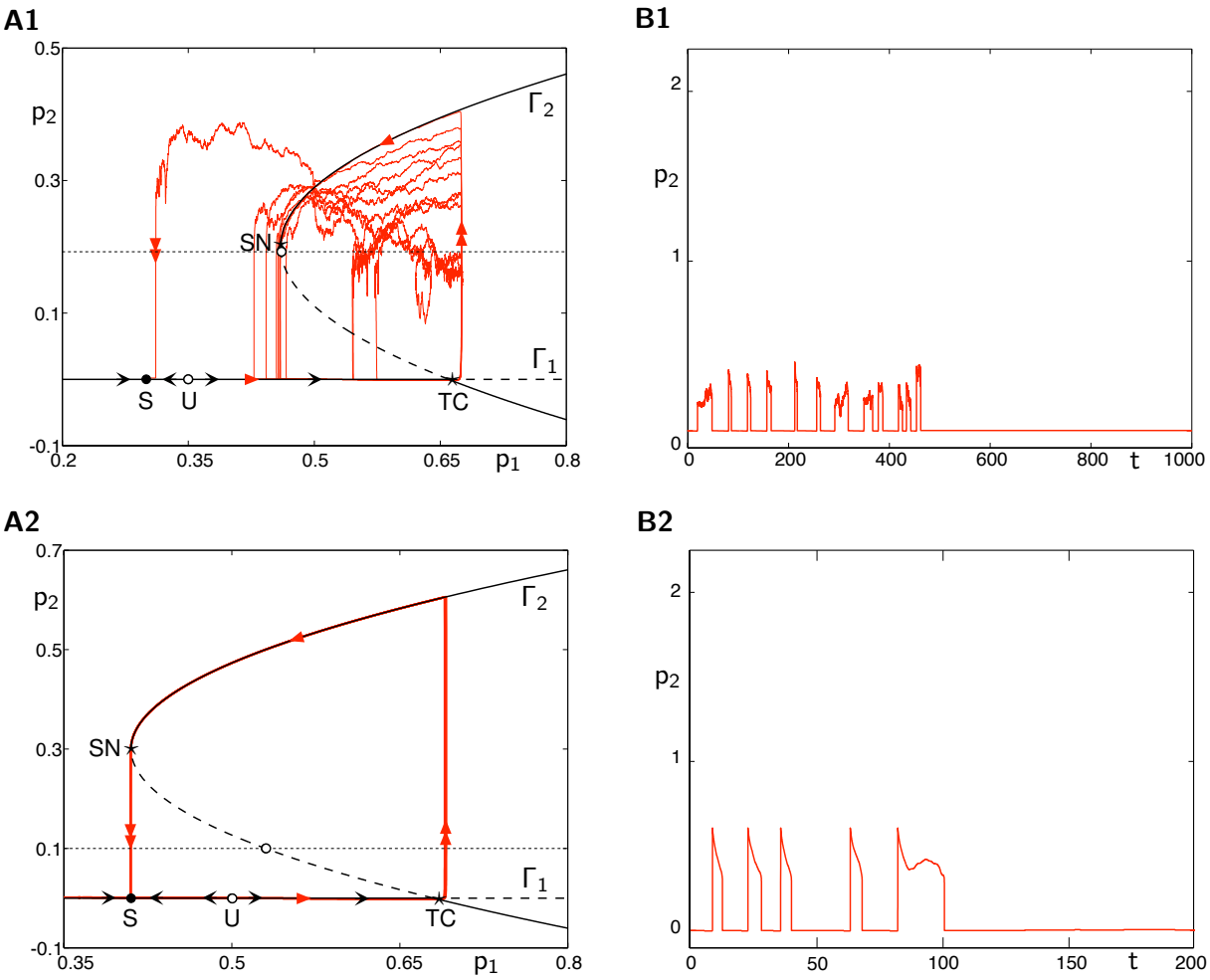

Figure S4:

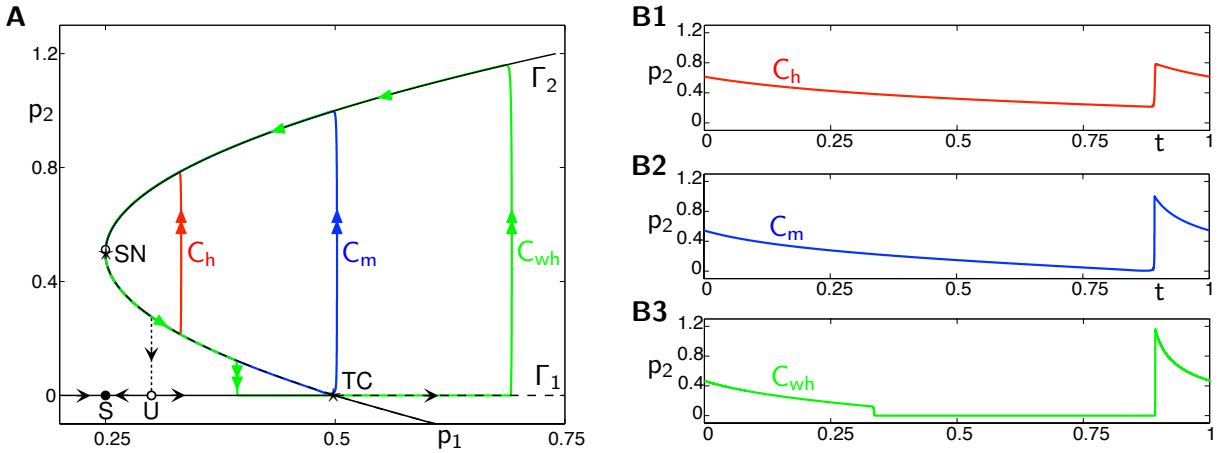

Figure S5:

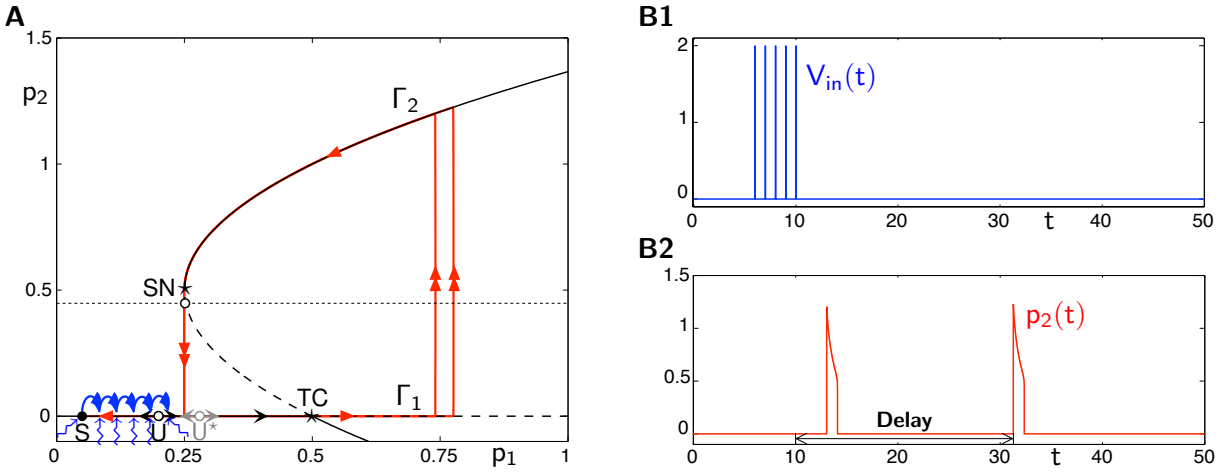

Figure S6: